# Interfacial Nanostructure and Hydrogen Bond Networks of Choline Chloride and Glycerol Mixtures Probed with X-ray and Vibrational Spectroscopies

Pyeongeun Kim[1], Chaya Weeraratna[1], Slavomír Nemšák[2], Nureshan Dias[1], Alexander K. Lemmens[1], Kevin R. Wilson[1], and Musahid Ahmed[1]*

[1] Chemical Sciences Division, Lawrence Berkeley National Laboratory, Berkeley, California 94720, USA

[2] Advanced Light Source, Lawrence Berkeley National Laboratory, Berkeley, California 94720, USA; Department of Physics and Astronomy, University of California Davis, Davis, California 95616, USA

email: mahmed@lbl.gov

## Abstract

The molecular distribution at the liquid-vapor interface and evolution of the hydrogen bond interactions in mixtures of glycerol and choline chloride are investigated using X-ray photoelectron spectroscopy (XPS) and Raman spectroscopy. Nanoscale depth profiles of supersaturated DES mixtures up to ~2 nm measured by ambient-pressure XPS shows the enhancement of choline cation ($Ch^+$) concentration by a factor of 2 at the liquid-vapor interface compared to the bulk. In addition, Raman spectral analysis of a wide range of DES mixtures reveals the conversion of gauche-conformer $Ch^+$ into the anti-conformer in relatively lower ChCl concentrations. Finally, the depletion of $Ch^+$ from the interface (probing depth = 0.4 nm) is demonstrated by aerosol-based velocity map imaging XPS measurements of glyceline and water mixtures. The nanostructure of liquid-vapor interfaces and structural rearrangement by hydration

can provide critical insight into the molecular origin of the deep eutectic behavior and gas capturing application of DESs.

**ToC Figure**
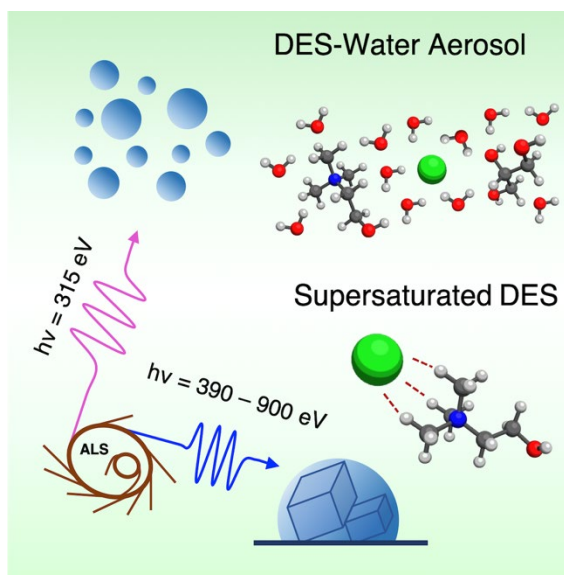
Deep eutectic solvents (DESs) are considered sustainable alternatives to conventional organic solvents and ionic liquids because of their affordability, biodegradability, and low toxicity.[1–4] DESs are not limited to being used as solvents, but are finding applications in gas capture[5–8] and thermal energy storage systems.[9–11] Most DESs consist of a hydrogen bond donor and an acceptor where their hydrogen bond interactions can significantly lower the freezing point of the solvent at specific compositions (*i.e.,* at the eutectic point).[12–15] Due to the complex inter- and intramolecular hydrogen bonding network, the physical characteristics of eutectic mixtures, such as viscosity, solvent polarity, and heat capacity, resemble those of ionic liquids and organic solvents.[1,13,16] The ability to tune these hydrogen bond interactions to target specific physical characteristics is what makes them particularly attractive.[17–19]

One of the most studied DESs is glyceline (melting point, m.p. = 233 K), a 1:2 molar mixture of Choline Chloride (ChCl, m.p. = 575 K) and Glycerol (Gly, m.p. = 291 K).[8,20–22] When mixed to form a DES, ChCl and Gly act as hydrogen bond acceptor and donor, respectively. There are numerous studies that aim to link these molecular interactions with the physical properties of glyceline, including but not limited to dynamic viscosity, structural relaxation, and heat capacity.[17,23–26] Notably, charge transfer and delocalization effects and the consequences on the hydrogen bonding network of this system remain unresolved and controversial.[27] Similar to the glycerol/water system, studied using X-Ray and vibrational spectroscopy,[28] nano-structuring, and phase separations are also present in glyceline.[28,29] Furthermore, when water is added to the system, hydration effects make it more challenging to understand an already complex intermolecular structure.[26,30–34] Therefore, gaining a molecular level understanding of interactions between ChCl and Gly is an important stepping stone on the path to designing and developing unique DESs for sustainable chemical processes in various industrial and environmental

applications.[35–38]

Diverse experimental tools have been used to increase our understanding of the hydrogen bond interactions and molecular properties leading to the distinctive properties of DESs. Turner and Holbrey utilized neutron diffraction measurements to develop a detailed picture of the hydrogen bond structures in glyceline, including extensive Gly$\cdots$Gly networks and bridged interactions of Ch$^+\cdots$Cl$^-\cdots$Gly.[29] Hydrogen bonds govern the molecular diffusion rate in DESs as shown in nuclear magnetic resonance (NMR) studies by D'Agostino et al,[39,40] while NMR was also used to probe these time-dependent hydrogen bond dynamics.[32,41] Raman and infrared (IR) spectroscopy, classic tools for probing hydrogen bond interactions through molecular vibrations, have been used to study the mechanism of DES formation[42] and the destructive effect of water on the extended hydrogen bond structures in DESs.[30,43,44]

In contrast, the interfacial molecular distribution of DESs is not as extensively studied compared to the intermolecular structures in the bulk solutions.[16] Gaining knowledge of this interfacial structure is important because the potential applications of DESs are directly related to the physicochemical properties at the interface. For example, understanding of the liquid-vapor interface is crucial in designing DES system for greenhouse gas capture.[5,6] Likewise, the liquid-solid interface plays a critical role in using DESs for extraction technologies.[18,19,45] While not extensive, there have been several experimental and simulation studies of the nanostructures in liquid-solid interface of DESs.[46–50] In case of the liquid-vapor (or gas) interface, however, there is a dearth of experimental studies to elucidate the interfacial behavior. Few computational studies have explored the orientation of hydrogen bond donors at the liquid-vapor interface.[51,52] Very recently, Gera et al. observed the water-induced depletion of urea and Ch$^+$ at the liquid-vapor interface of reline (i.e., a 1:2 mixture of ChCl and urea) using Sum Frequency Generation (SFG)

and Attenuated Total Reflection Fourier Transform Infrared Spectroscopy (ATR-FTIR).[53]

In this paper, dilute to supersaturated compositions of binary ChCl and Gly as well as ternary mixtures with water will be examined by complementary spectroscopic techniques to understand how the evolution of the hydrogen bond network and interfacial properties are correlated.[54] The molecular distribution of $Ch^+$ and Gly at liquid-vapor interface will be examined by ambient-pressure X-ray photoelectron spectroscopy (AP-XPS) of supersaturated ChCl and Gly mixtures and corresponding depth profiles on the nanoscale will be determined by tuning the X-Ray photon energy. The changes in hydrogen bond interactions and molecular conformation of $Ch^+$ will be provided by the Raman spectral analysis of varying molar ratios of ChCl and Gly mixtures. Finally, to unravel the effect of water on the liquid-vapor interface of glyceline, results from surface-sensitive velocity map imaging (VMI) XPS of glyceline and water mixtures will be presented.[55]

C 1s X-ray photoelectron spectra and the Gaussian deconvolution of 3:1 and 5:1 supersaturated ChCl:Gly mixtures are shown in **Figure 1**. We note that the initial mixing molar ratios of 3:1 and 5:1 does not represent the actual molar ratios of samples under analysis because the mixtures include both solid and liquid phases. The solid phase of the mixture is undissolved ChCl. Photoelectron spectra presented here represent only the liquid phase since the X-ray beam only interacts with the outermost liquid layer of the supersaturated mixture samples. In **Figure 1a** and **1b** two two peaks and a shoulder are clearly discernable from the spectra at the lower photon energies (hv = 390 and 480 eV), which can be translated to 3 peaks in the Gaussian fitting. These three Gaussian peaks centered at 286.0, 287.3, and 288.8 eV binding energy (BE) are assigned as quaternary ammonium C (C-N$^+$), alcohol C (C-O), and gas phase alcohol C (C-O), respectively. These assignments are in line with the XPS binding energy data of C-N$^+$ and C-O from the

literature.[56–58]

To further verify the peak assignments, velocity map imaging XPS measurements were performed on reference samples - for pure glycerol and glyceline (ChCl:Gly = 1:2) aerosols at hv = 325 eV as shown in **Figure S1**. Clearly, the shoulder near 285.9 eV appears in the XPS spectrum of glyceline aerosol, which is absent in the spectrum of pure Gly aerosol (**Figure S1**). The quantitative values of intensity (a), position (b), and width (c) parameters used for Gaussian deconvolution of AP-XPS data are tabulated in SI Table I. The consistently larger intensities of the 286.0 eV (C-N$^+$) peak with varying photon energies (**Figure 1b**) are consistent with the 5:1 mixture having a higher ChCl content compared to the 3:1 mixture, thus a higher degree of supersaturation is achieved in the 5:1 mixture as one can expect.

**Figure 1** also clearly demonstrates the decrease of C-N$^+$ peak as the X-ray energy increases from 390 to 900 eV in both mixtures. The energy of the incident photon determines the kinetic energy of excited photoelectrons, which is related to the probing depth of the measurements. Photons with higher energy generate photoelectrons with larger kinetic energy, leading to a larger inelastic mean free path (IMFP).[59] Using the universal curve equation, one can estimate the IMFP of photoelectrons as a function of kinetic energy and average atomic number of the system.[60] Moreover, the integrated area of C-N$^+$ and C-O peaks can be translated into the molar ratio of Ch$^+$ and Gly by accounting for the contribution from each species: Ch$^+$ contains 4 C-N$^+$ and 1 C-O while Gly consists of 3 C-O carbons (**Figure 1c**). Therefore, if the molar ratio of Ch$^+$ and Gly in the solution is $x$ to $1$-$x$, $x$ can be obtained by solving the following equation at each probing depth.

$$Area(C - N^+) : Area(C - O) = \frac{4x}{3-2x} \qquad (1)$$

The resulting depth profiles of $Ch^+$ to Gly ratio acquired from the AP-XPS spectra are shown in **Figure 1d**. The probing depth, *i.e.*, the IMFP of photoelectrons, of each measurement is given in nanometer (nm) scale.

Here, the decrease of $Ch^+$ content with respect to the Gly was observed in both supersaturated mixtures. This behavior may arise from the different hydrogen bond interactions near the surface and the bulk of the supersaturated mixtures. Unlike dilute ChCl:Gly mixtures, supersaturated mixtures probed by AP-XPS in this study are abundant with chloride anions ($Cl^-$). At the liquid-vapor interface of glycerol, the concentration of $Cl^-$ can be enhanced at the outermost region of the interface within 0.5 nm according to a recent neutral impact collision ion scattering spectroscopy result by Kumar et al.[61] In addition, they revealed that the surface propensity of $Cl^-$ is independent of the counterions, leading us to infer that $Cl^-$ can be enhanced at the liquid-vapor interface in our system of interest (ChCl and Gly).[61] Concurrently, $Cl^-$ at the interface can effectively interact with C-H of choline cations through halogen-hydrogen bonding forming ion pairs, thus producing higher XPS signal of $C-N^+$ near the surface.[62]

This argument is further supported by formation of a series of doublets shifted to lower BE in the AP-XPS spectra of $Cl^-$ in the higher X-ray energy as shown in **Figure S2**. AP-XPS measurements of O 1s and N 1s core-levels with Gaussian deconvolution are also presented in **Figure S3** and **S4**. For $Cl^-$ AP-XPS, only one pair of doublets from spin-orbit interaction of $Cl^-$ ($2p_{1/2}$ and $2p_{3/2}$) can be observed in the spectra near the interface (hv = 390 and 480 eV, <1nm depth). However, the rise of a new pair of doublets which is red-shifted by ~1.2 eV is clearly discernable for higher energy spectra (hv = 735 and 900 eV, >1.5 nm depth). This red-shifted doublet is an indicator for the $Cl^-$ participating in the relatively weaker interaction with Gly compared to $Ch^+\cdots Cl^-$. According to the XPS study of NaCl solution by Ammann *et al.*, a red-

shift of 1.8 eV was observed between frozen and liquid solutions.[63] This observation agrees with our result where solvation of ion pairing leads to the BE red-shift of Cl 2p doublets (this work: $Ch^+ \cdots Cl^-$ / Ammann *et al.*: $Na^+ \cdots Cl^-$). The difference in red-shift values (~1.2 eV vs 1.8 eV) may be due to the different interaction of $Cl^-$ with counterions ($Ch^+$ vs $Na^+$). Accordingly, one can visualize that at the interface, the $Cl^-$ ions are strongly bound to $Ch^+$, and this ion paring is interrupted by Gly a few nanometers below the interface. This experimentally observed nanometer-scale heterogeneity at the liquid-vapor interface of ChCl and Gly mixtures suggests that the interfacial enhanced $Cl^-$ and $Ch^+$ could play a role in gas-DES interactions relevant to technological applications. Therefore, when designing a DES system for gas capturing, the interfacial properties of hydrogen bond donor should be thoroughly evaluated.

To investigate the changes in the hydrogen bonding network as a function of ChCl content, a series of Raman spectra were measured for varying molar ratio mixtures of ChCl:Gly; ranging from dilute (1:3) to supersaturated (5:1) as well as pure ChCl and Gly. Two different regions ($600 – 1400$ cm$^{-1}$ and $2700 – 3300$ cm$^{-1}$) of the Raman spectra are presented in **Figure 2**. Raman spectra below $600$ cm$^{-1}$ are displayed in **Figure S5**. In the $600 – 1400$ cm$^{-1}$ range of the spectrum (**Figure 2a**), characteristic vibrations of pure liquid Gly include COH out of plane (op) wagging at ~680 cm$^{-1}$, C-O stretching at ~810 cm$^{-1}$, C-C-C symmetric stretching at ~840 cm$^{-1}$, C-O stretching at ~920 cm$^{-1}$, C-O-H scissoring at ~970 cm$^{-1}$, C-O stretch at ~1050 and 1120 cm$^{-1}$, and $CH_2$ bending coupled with COH scissoring at ~1250 cm$^{-1}$.[42] Signatures of $Ch^+$ vibrational peaks from pure ChCl include a sharp $N-C_4$ symmetric stretch at ~715 cm$^{-1}$, asymmetric $N-C_4$ stretches at ~860, 900, and 940 cm$^{-1}$, C-C stretch at ~1040 cm$^{-1}$, and a C-O stretch at ~1080 cm$^{-1}$ (**Figure 2a**).[42] For every mixture, the Raman spectra show characteristic peaks from both compounds with a weighted intensity contribution from each compound depending on the mixing

ratio.

However, the Raman spectra of the mixtures are not simply a linear combination of ChCl and Gly spectra. It is clearly noticeable in **Figure 2a** that the small peak near 760 cm$^{-1}$ emerges in relatively dilute mixtures (1:3, 1:2, and 1:1). Notably, the 760 cm$^{-1}$ feature does not belong to characteristic vibrations of pure ChCl or Gly but arises from the C-N stretching mode of the anti-conformer, as opposed to the strong N-C$_4$ symmetric stretch of the gauche-conformer at ~715 cm$^{-1}$.[64,65] This anti-conformer peak of Ch$^+$ has been observed in aqueous solutions of ChCl and choline dihydrogen phosphate ([Ch][DHP]) salts as well.[66–68] The intensity ratios of anti (760 cm$^{-1}$) to gauche (715 cm$^{-1}$) versus mixing ratio of ChCl:Gly are displayed in **Figure 3**.

In pure ChCl, the gauche-conformer C-N stretch peak is predominant because of the interactions between Cl$^-$ and Ch$^+$, which is thermodynamically favorable in the gauche geometry (two C-H$\cdots$Cl$^-$ and O-H$\cdots$Cl$^-$).[62] On the other hand, in dilute mixtures (1:3, 1:2, and 1:1) Ch$^+$ ions are dissolved by Gly and form hydrogen bond networks through donor (Gly) – acceptor (Ch$^+$) interactions, and weaken the interaction between Cl$^-$ and Ch$^+$. It is known that Cl$^-$ can also act as a hydrogen bond bridge between Ch$^+$ and Gly.[69] Therefore, the structural relaxation of ChCl due to the hydrogen bond donor-acceptor interactions result in the formation of anti-conformer Ch$^+$ ions in relatively dilute mixtures.[66] It is interesting that as the concentration of ChCl in the mixture increases and reaches supersaturated states (3:1 and 5:1), the anti-conformer peak near 760 cm$^{-1}$ disappears and the gauche peak at 715 cm$^{-1}$ dominates. Due to the crystalline-dominated phase of these supersaturated mixtures (**Figure S8**), the major contribution to the obtained Raman signal is from the ChCl crystal. This observation also suggests that the dominating hydrogen bond interaction in supersaturated mixtures are between Ch$^+\cdots$Cl$^-$ rather than Ch$^+\cdots$Gly or Ch$^+\cdots$Cl$^-$ $\cdots$Gly. As suggested by Faraone *et al*, the deep-eutectic behavior diminishes in supersaturated

mixtures because the hydrogen bonding network of Gly, which is essential for deep eutectic character of glyceline, is broken by a high concentration of ChCl.[24]

Spectral features from the higher wavenumber region (2700 – 3300 cm$^{-1}$) in **Figure 2b** also provide valuable information about the evolution of hydrogen bond interactions. For the pure Gly spectrum, only two peaks near 2880 and 2950 cm$^{-1}$ are discernable, which can be assigned to the $CH_2$ symmetric and asymmetric stretch, respectively. On the other hand, the pure ChCl spectrum shows more complex features from 2800 to 3030 cm$^{-1}$ due to multiple C-H vibrational modes. In general, peaks with frequency larger than 2950 cm$^{-1}$ represent symmetric stretch vibrations of $CH_2$ and $CH_3$, and peaks below 2950 cm$^{-1}$ arise from asymmetric stretching of $CH_2$ and $CH_3$.[42] In dilute mixtures of ChCl and Gly (1:3 and 1:2), the single asymmetric $CH_3$ stretching peak near 3020 cm$^{-1}$ from $Ch^+$ and splitting of $CH_2$ asymmetric stretching of Gly near 2950 cm$^{-1}$ were observed.

Interestingly, the 3220 cm$^{-1}$ peak of ChCl appears in supersaturated mixtures (3:1 and 5:1), which can be assigned to the O-H vibration hydrogen-bonded to $Cl^-$ (O-H$\cdots Cl^-$).[70] By comparing this spectral change with lower wavenumber spectra (**Figure 2a**), it is evident that the intensity changes of O-H$\cdots Cl^-$ peak at 3220 cm$^{-1}$ and anti-conformer $Ch^+$ peak at 760 cm$^{-1}$ are anticorrelated, *i.e.*, 3220 cm$^{-1}$ peak appears after the 760 cm$^{-1}$ peak has disappeared. This relationship is clearly shown in **Figure 3**. Therefore, the peak at 3220 cm$^{-1}$ can be the indicator for strong $Ch^+\cdots Cl^-$ interactions, which result from the dominating gauche-conformer $Ch^+$ in the supersaturated mixtures discussed earlier.

To gain further insight about the effect of water on the interfacial nanostructure of glyceline, a series of XPS spectra were collected from aerosols generated from pure glyceline and from water mixtures (30, 50, 80 wt% $H_2O$), and presented in **Figure 4a**. The probing depth of these measurements was ~0.4 nm, as estimated from the electron kinetic energy of ~27 eV.[60] It is

clearly seen in **Figure 4a** that the addition of water to glyceline decreases the C-N$^+$ peak, which reflects the withdrawal of Ch$^+$ from the surface into the bulk. The peak areas of XPS spectra can be converted into molar ratio of Ch$^+$ to Gly using equation (1) discussed earlier. The Ch$^+$ to Gly ratios at the aerosol interface as a function of water content in the mixtures are displayed in **Figure 4b**. The fitting parameters for Gaussian analysis are given in SI Table II. For glyceline (0 wt% water), it is possible that the interfacial Ch$^+$ content is lower than what is expected because the surface may be populated with Cl$^-$ as discussed in the earlier section.[61] It can be inferred from the glyceline aerosol spectrum that unlike supersaturated mixtures, the Ch$^+\cdots$Cl$^-$ interaction is not the dominant one at the interface. Given that the probing depth of aerosol XPS measurements is close to a thin molecular monolayer (~0.4 nm),[46] the XPS spectra in **Figure 4a** underrepresent the Ch$^+$ content of the entire aerosol volume. It should also be noted that the given wt% of water was defined in the solution phase, and the actual water content of the aerosol can be lower than the initial values because the interaction of aerosols and X-ray takes place inside the vacuum chamber and there will also be evaporation in the aerodynamic lens system.

This unexpected depletion of Ch$^+$ at the liquid-vapor interface can be explained by the role of water and hydration of ions in DES-water mixtures. In glyceline, the hydrogen bond networks between Ch$^+$ and Gly are bridged by Cl$^-$ according to a molecular dynamics (MD) simulation study by Weng et al.[69] However, when water molecules are introduced, the stronger hydrogen bond interaction between Cl$^-$ and water starts to dominate the system, thus breaking the established Ch$^+\cdots$Cl$^-\cdots$Gly network. Furthermore, Cl$^-$ is not known to be particularly enhanced at the air-liquid interface of aqueous solutions as opposed to the case of Cl$^-$ in glycerol discussed earlier.[61,71] Therefore, addition of water is expected to decrease the enhancement of Cl$^-$ concentration at the vapor-liquid interface of glyceline aerosols through the hydration of Cl$^-$. As a result, Ch$^+$ at the

surface can also be guided from the surface into bulk by hydration, which can be a more thermodynamically favorable process.[69] The qualitative effect of water to the interfacial distribution of $Ch^+$ and Gly is also consistently observed in aerosols generated from 1:1 and 1:3 ChCl:Gly and water mixtures as shown in the C 1s XPS spectra (**Figure S6**). It should be noted that although not enhanced, $Cl^-$ is not completely depleted from the aerosol interface, as the Cl 2p signal was observed in all XPS spectra of water mixtures (**Figure S7**). Therefore, the depletion of ions from the interface due to hydration is more significant for $Ch^+$ than $Cl^-$.

The results presented in **Figure 4** provide additional insights to the current understanding of hydration of DESs, especially for $Ch^+$. In particular, an air-DES interfacial study of reline (ChCl:urea = 1:2) and water mixtures by Gera et al. shows that increasing water content in the system depletes $Ch^+$ from the surface above 40 wt% $H_2O$.[53] Their results from vibrational SFG spectroscopy have indicated the surface of the mixture above 60 wt% $H_2O$ resemble the spectrum of pure water.[53] This observation agrees with our result from aerosol XPS spectra (**Figure 4b**). The XPS spectrum of 80 wt% $H_2O$ mixture (**Figure 4a**) is almost indistinguishable from the spectrum of pure glycerol (**Figure S1**) or glycerol-water mixtures, indicating minor surface presence of $Ch^+$ at higher water content.[28] Therefore, these surface behavior of $Ch^+$ in two distinct DESs (glyceline and reline) suggests the interaction between hydrogen bond acceptor and water ($Ch^+\cdots H_2O$) can be the driving force of observed $Ch^+$ depletion from the liquid-vapor interface. This hypothesis is similar to the effect of water in bulk systems, where the water-induced rearrangement of hydrogen bond interaction in DESs have been consistently attributed to the increasing $Ch^+\cdots H_2O$ interactions.[30–32]

Both results from AP-XPS measurement of supersaturated binary mixtures (**Figure 1**) and aerosol XPS of ternary mixtures with water (**Figure 4**) provide unique yet complementary

information about the liquid-vapor interface of the DES system under investigation. Possible molecular distribution of Gly, $Ch^+$, $Cl^-$, and $H_2O$ along the liquid-vapor interface to bulk according to our spectroscopic observation is visualized in **Figure 5**. In the case of a supersaturated mixture (**Figure 5a**), the enhancement of the $Cl^-$ concentration at the surface results in the $Cl^- \cdots Ch^+$ interaction to be dominant at the liquid-vapor interface, whereas a weaker $Cl^- \cdots Gly$ interaction can be found further away from the interface. In comparison, the addition of water to glyceline causes restructuring of the established $Ch^+ \cdots Cl^- \cdots Gly$ network by hydration (**Figure 5b**). As a result, the interface of the water-glyceline mixture is mainly comprised of Gly, $H_2O$, and $Cl^-$ while hydrated $Ch^+$ ions are depleted from the surface.

The interfacial properties and hydrogen bond interactions in glyceline, a benchmark DES system, were probed by using a portfolio of spectroscopic techniques. AP-XPS, Raman spectroscopy, and aerosol based VMI XPS measurements were used to probe the molecular and atomic distribution at the liquid-vapor interface and hydrogen bond structures of binary ChCl and Gly mixtures as well as ternary mixtures with water. In supersaturated mixtures (3:1 and 5:1 ChCl:Gly), liquid phase depth profiles of $C-N^+$ and $C-O$ from AP-XPS measurements revealed the increase of $Ch^+$ concentration at the liquid-vapor interface possibly due to the surface propensity of $Cl^-$ in glycerol. Raman spectroscopic analysis was carried out for a wide range of ChCl and Gly mixtures to understand the changes in intermolecular interactions as a function of mixing ratio. It was found that in relatively dilute mixtures (1:3 to 1:1), the absence of the strong $Ch^+ \cdots Cl^-$ interaction leads to the formation of the anti-conformer of $Ch^+$. Meanwhile in supersaturated mixtures, gauche-conformer $Ch^+$ was predominant due to the strong $Ch^+ \cdots Cl^-$ interaction as indicated by the $O-H \cdots Cl^-$ peak. Finally, to visualize the effect of water on the liquid-vapor interface of glyceline aerosols were investigated by VMI XPS spectroscopy. Addition of water to

this DES system led to the rearrangement of hydrogen bond structures, and depletion of $Ch^+$ from the surface of the aerosol was observed.

This study expands the knowledge of not only the interface and intermolecular structures of glyceline, but of the supersaturated ChCl and Gly mixtures and ternary mixtures with water. Our observations provide fundamental insights into the hydrogen bond interactions between molecular ions, atomic anions, and polar molecules when their compositions change. In addition, we have shown that molecular distribution of the liquid-vapor interface of a DES system can be different from the bulk, which impact the gas adsorption behavior. Therefore, we propose that the interface of the hydrogen bond donor-acceptor pair of DESs as well as their interaction with water must be thoroughly considered when designing novel DESs for more sustainable chemical processes. Future studies of the DES systems with different hydrogen bond donors (e.g., reline – ChCl and urea) will likely provide additional information about the relationship between interfacial nanostructure and hydrogen bond interactions. Furthermore, MD simulations of large molecular systems of DESs could deliver dynamics of ions and molecules at the interface, which would greatly benefit and complement the experimental study presented in this paper.

**Experimental Methods**

Glycerol (>99%) and choline chloride (>99.0%) were purchased from Sigma Aldrich and used without further purification. Relatively dilute mixtures (1:3, 1:2, 1:1) form homogeneous liquids whereas supersaturated mixtures (3:1 and 5:1) coexist with liquid and ChCl crystals (**Figure S8**). For water mixtures of glyceline, ultrapure water (Milli-Q, 18.2 MΩ·cm) was used to dissolve ChCl and Gly (1:2) with 30, 50, and 80 wt% $H_2O$.

AP-XPS measurements were performed at beamline 9.3.2 of the Advanced Light Source (ALS) synchrotron. A detailed description of AP-XPS can be found in previous publications using this instrument.[72,73] Only supersaturated mixtures were subject to AP-XPS measurements because viscosity allowed the sample to be placed stably on the vertically mounted silicon substrate in the instrument. A picture of 3:1 and 5:1 ChCl:Gly mixtures and their survey photoelectron spectra with 735 eV X-ray excitation energy are presented in **Figure S9**. The photoelectron signal from silicon (Si) substrate, Cl 2p, C 1s, N 1s, and O 1s can be clearly identified from the spectra. The strong Si signal near 100 eV, especially for the 5:1 mixture (**Figure S9**), indicates that the droplet under examination was smaller than the size of the X-ray beam of ~1 mm in diameter.

Raman spectroscopic measurements of pure Gly, pure ChCl, and a range of mixtures (1:3 to 5:1) in glass vials were made using a Spectra Solutions Inc. laser probe consisting of a 532 nm Nd:YAG CW laser with 82 mW average power (Opto Engine). The Stokes-shifted Raman signal was collected in orthogonal geometry, and recorded with a spectrometer equipped with a volume-pass holographic grating (Spectra Solutions Inc.) and thermoelectric-cooled charged coupled detector (Andor) with 1650x200 pixels (4 cm$^{-1}$ resolution). Integration time for each measurement was 5 seconds. The excitation laser and collected Raman signal were both coupled via optical fibers.

Aerosol-based VMI XPS measurements were performed at beamline 9.0.1 at the ALS. Details of the VMI photoelectron spectrometer are described in previous papers from our group.[55,74] In short, aerosols are generated from the atomizer (TSI Model 3076) filled with glyceline-water mixtures with varying water content and introduced to the instrument by an aerodynamic lens and differential pumping. Pure glycerol and glyceline aerosols were produced through nucleation by heating the liquid in a tube furnace (160 °C), while room temperature

carrier gas ($N_2$) flows through the headspace of the liquid-containing tube. Photoelectrons were generated at the interaction region, and the velocity map images were collected from a phosphor screen-microchannel plate-camera detector configuration. A continuous stream of aerosol beam provides fresh samples of interest free of X-ray damage similar to liquid jet XPS experiments. The resulting C 1s XPS spectra of pure Gly and glyceline (1:2 ChCl:Gly) aerosols are shown in **Figure S1**.
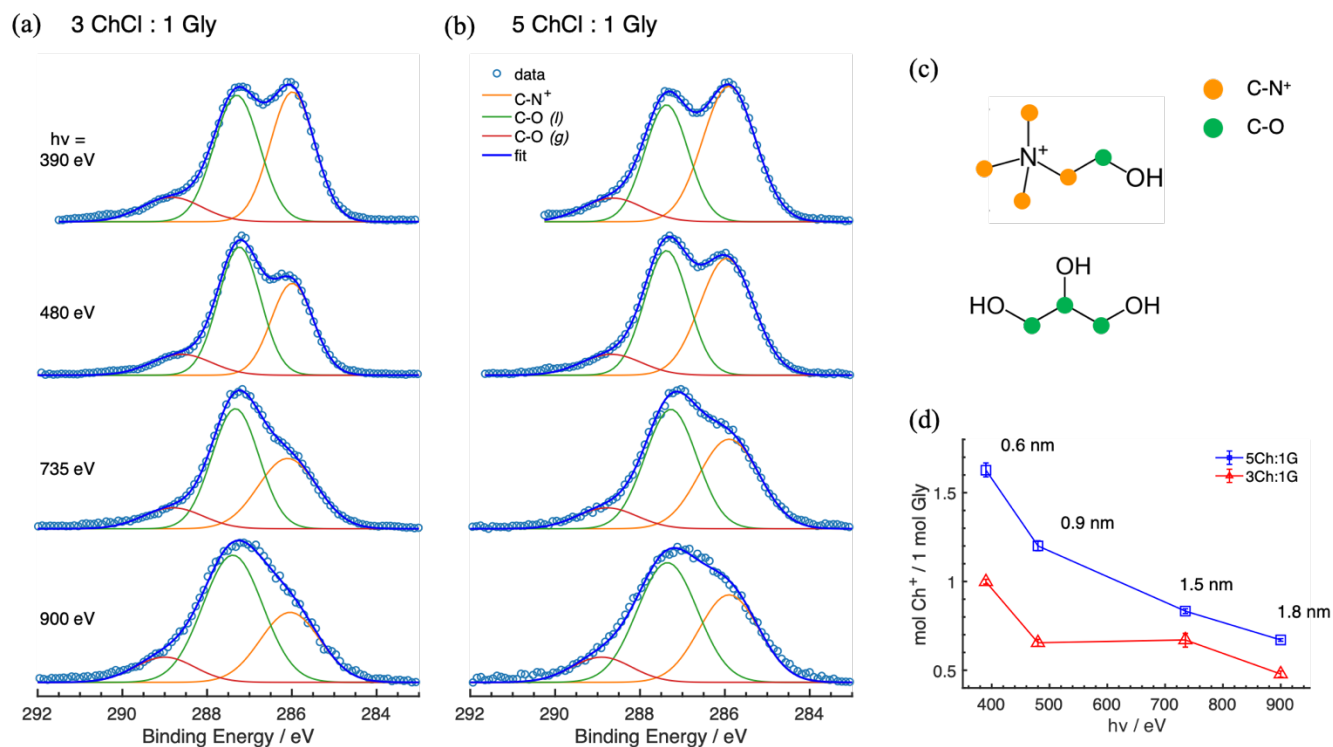
**Figure 1.** C 1s AP-XPS spectra collected for (a) 3:1 and (b) 5:1 ChCl:Gly mixtures with X-ray photon energies (hν) of 390, 480, 735 and 900 eV. C-N$^+$ peak is centered at 286.0 eV (solid orange line). Liquid (solid green line) and gas phase C-O peaks (solid red line) are located at 287.3 and 288.8 eV, respectively. (c) Contribution from different carbon species to the XPS spectra highlighted in molecular structures of Ch$^+$ and Gly (orange dots: C-N$^+$ and green dots: C-O). (d) Depth profile of Ch$^+$ to Gly ratio versus X-ray energy in 5:1 (blue square) and 3:1 (red triangle) supersaturated ChCl:Gly mixtures. Solid lines are guides to the eye. Error bars represent 95% confidence of Gaussian fitting.
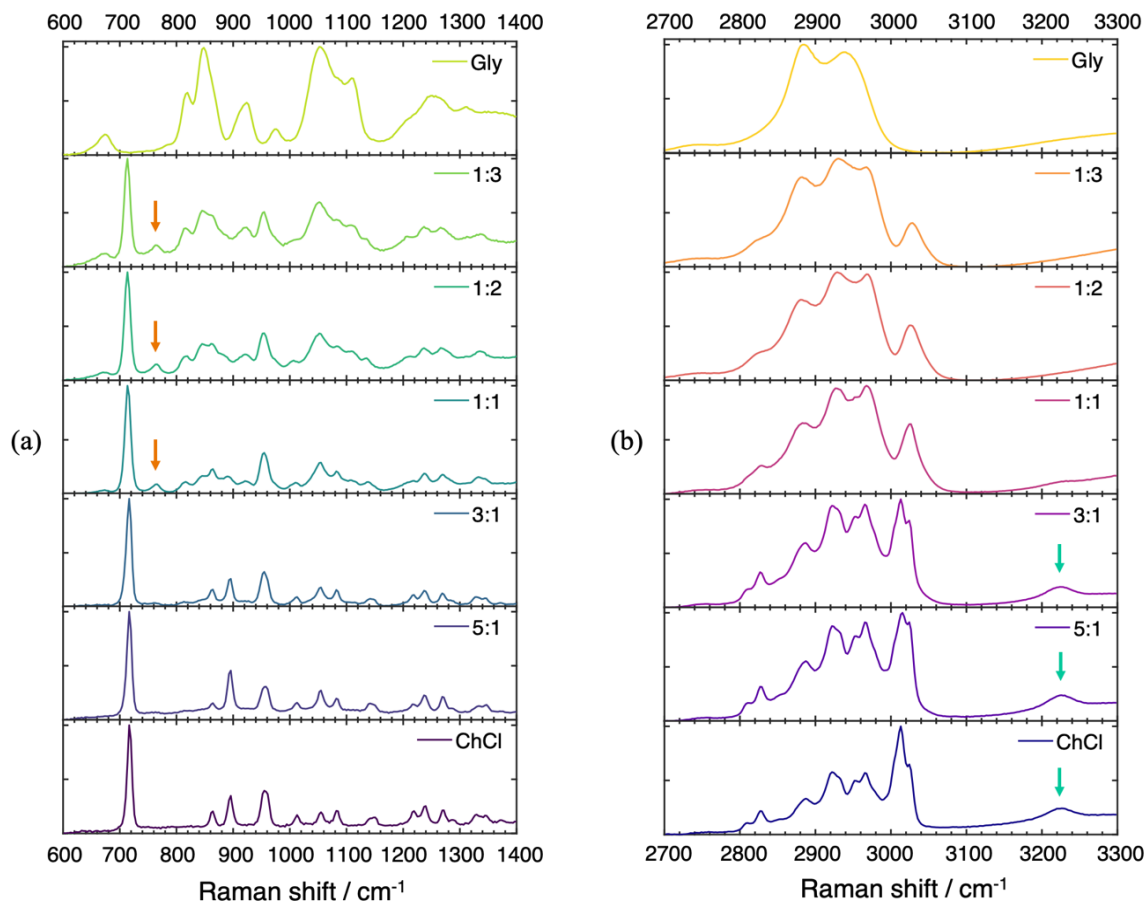
**Figure 2.** Vibrational Raman spectra of full-range ChCl:Gly mixtures normalized to the maximum intensity. (a) Lower frequency at $600 - 1400$ cm$^{-1}$ and (b) higher frequency spectra at $2700 - 3300$ cm$^{-1}$ are shown separately. Orange arrows on (a) are added to highlight formation of anti-conformer Ch$^+$ peak at 760 cm$^{-1}$. On (b) green arrows indicate a rise of a strong O-H$\cdots$Cl$^-$ interaction peak from supersaturated mixtures as well as solid state ChCl.
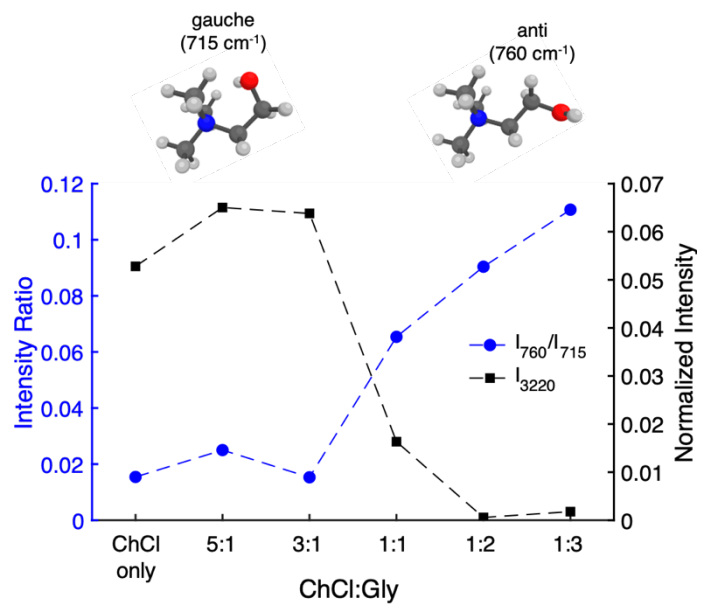
**Figure 3.** Raman intensity ratio of anti- to gauche-conformer peaks of $Ch^+$ (filled blue circle, $I_{760}/I_{715}$) and normalized intensity of O-H$\cdots$Cl- peak (filled red square, $I_{3220}$) versus mixing ratio of ChCl:Gly. Dashed lines are guides to the eye. Structures of both $Ch^+$ conformers are shown above the graph.
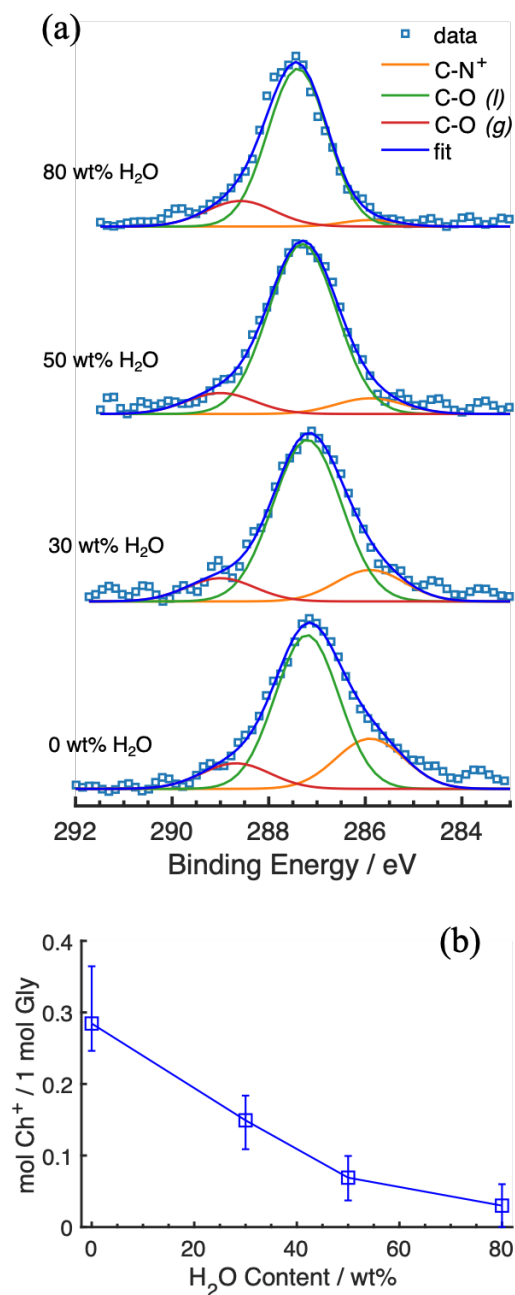
**Figure 4.** (a) Aerosol XPS spectra and Gaussian deconvolution of pure glyceline (ChCl:Gly=1:2) and water mixtures at hv = 315 eV (probing depth ~ 0.4 nm). (b) $Ch^+$ to Gly ratio versus $H_2O$ content in glyceline and water mixture aerosols surface. Error bars represent 95% confidence of the Gaussian fit.
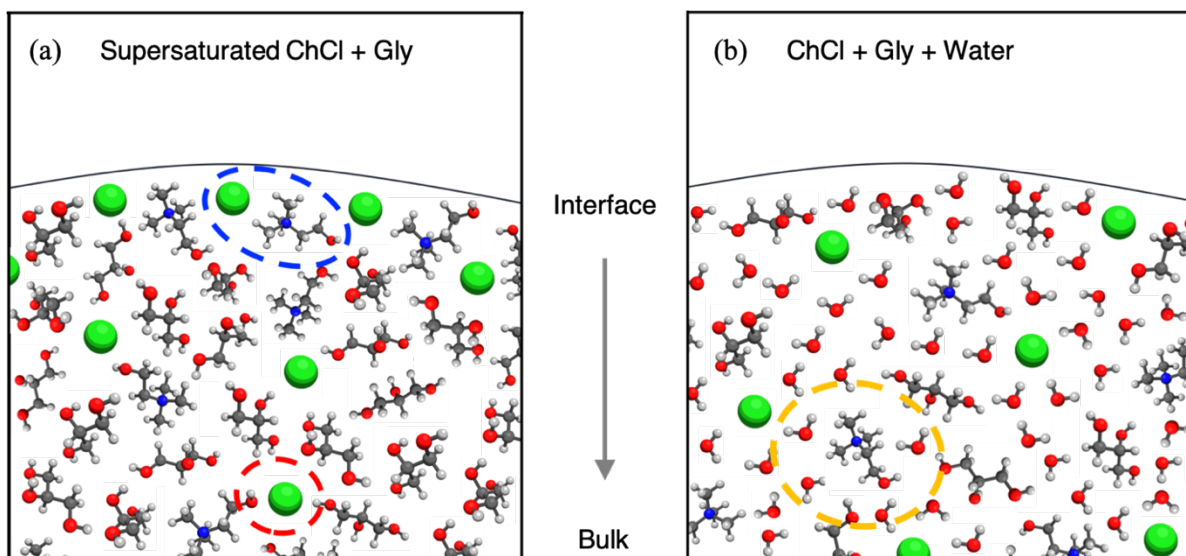
**Figure 5.** Schematic illustrations of (a) supersaturated ChCl and Gly mixture and (b) glyceline-water mixtures at a liquid-vapor interface. On panel (a), the enhancement of Cl$^-$ and the strong Ch$^+$...Cl$^-$ interaction (dashed blue oval) near the interface are displayed. Deeper in the bulk, the bridged Ch$^+$···Cl$^-$···Gly interaction is highlighted in dashed red oval. On (b), depletion of Ch$^+$ from the interface by hydration is depicted in dashed orange oval.

**Acknowledgements**

**Associated Content**

**Supporting Information**

Picture of prepared samples, survey AP-XPS spectra of supersaturated mixtures, additional AP-XPS spectra (N 1s, O 1s, and Cl 2p), Raman spectra below 600 cm$^{-1}$, aerosol XPS spectra of ternary mixtures (1:1 and 1:3 ChCl:Gly with water), and tabulated Gaussian fitting parameters for C 1s XPS spectra (PDF).

# References

(1) Abbott, A. P.; Harris, R. C.; Ryder, K. S.; D'Agostino, C.; Gladden, L. F.; Mantle, M. D. Glycerol Eutectics as Sustainable Solvent Systems. *Green Chem.* **2011**, *13*, 82–90.

(2) Kaur, S.; Kumari, M.; Kashyap, H. K. Microstructure of Deep Eutectic Solvents: Current Understanding and Challenges. *J. Phys. Chem. B* **2020**, *124*, 10601–10616.

(3) Hansen, B. B.; Spittle, S.; Chen, B.; Poe, D.; Zhang, Y.; Klein, J. M.; Horton, A.; Adhikari, L.; Zelovich, T.; Doherty, B. W.; Gurkan, B.; Maginn, E. J.; Ragauskas, A.; Dadmun, M.; Zawodzinski, T. A.; Baker, G. A.; Tuckerman, M. E.; Savinell, R. F.; Sangoro, J. R. Deep Eutectic Solvents: A Review of Fundamentals and Applications. *Chem. Rev.* **2021**, *121*, 1232–1285.

(4) Hammond, O. S.; Mudring, A.-V. Ionic Liquids and Deep Eutectics as a Transformative Platform for the Synthesis of Nanomaterials. *Chem. Commun.* **2022**, *58*, 3865–3892.

(5) Pelaquim, F. P.; Barbosa Neto, A. M.; Dalmolin, I. A. L.; Costa, M. C. D. Gas Solubility Using Deep Eutectic Solvents: Review and Analysis. *Ind. Eng. Chem. Res.* **2021**, *60*, 8607–8620.

(6) Shen, Y.; Abedin, R.; Hung, F. R. On the Performance of Confined Deep Eutectic Solvents and Ionic Liquids for Separations of Carbon Dioxide from Methane: Molecular Dynamics Simulations. *Langmuir* **2019**, *35*, 3658–3671.

(7) Chen, Y.; Han, X.; Liu, Z.; Yu, D.; Guo, W.; Mu, T. Capture of Toxic Gases by Deep Eutectic Solvents. *ACS Sustainable Chem. Eng.* **2020**, *8*, 5410–5430.

(8) García, G.; Aparicio, S.; Ullah, R.; Atilhan, M. Deep Eutectic Solvents: Physicochemical Properties and Gas Separation Applications. *Energy Fuels* **2015**, *29*, 2616–2644.

(9) Shahbaz, K.; AlNashef, I. M.; Lin, R. J. T.; Hashim, M. A.; Mjalli, F. S.; Farid, M. M. A Novel Calcium Chloride Hexahydrate-Based Deep Eutectic Solvent as a Phase Change Materials. *Sol. Energy Mater. Sol. Cells.* **2016**, *155*, 147–154.

(10) Abedin, R.; Shen, Y.; Flake, J. C.; Hung, F. R. Deep Eutectic Solvents Mixed with Fluorinated Refrigerants for Absorption Refrigeration: A Molecular Simulation Study. *J. Phys. Chem. B* **2020**, *124*, 4536–4550.

(11) Florindo, C.; Romero, L.; Rintoul, I.; Branco, L. C.; Marrucho, I. M. From Phase Change Materials to Green Solvents: Hydrophobic Low Viscous Fatty Acid–Based Deep Eutectic Solvents. *ACS Sustainable Chem. Eng.* **2018**, *6*, 3888–3895.

(12) Abbott, A. P.; Capper, G.; Davies, D. L.; Rasheed, R. K.; Tambyrajah, V. Novel Solvent Properties of Choline Chloride/Urea mixtures *Chem. Commun.* **2003**, No. 1, 70–71.

(13) AlOmar, M. K.; Hayyan, M.; Alsaadi, M. A.; Akib, S.; Hayyan, A.; Hashim, M. A. Glycerol-Based Deep Eutectic Solvents: Physical Properties. *J. Mol. Liq.* **2016**, *215*, 98–103.

(14) Khajeh, A.; Shakourian-Fard, M.; Parvaneh, K. Quantitative Structure-Property Relationship for Melting and Freezing Points of Deep Eutectic Solvents. *J. Mol. Liq.* **2021**, *321*, 114744.

(15) Van Den Bruinhorst, A.; Costa Gomes, M. Is There Depth to Eutectic Solvents? *Curr. Opin. Green Sustain. Chem.* **2022**, *37*, 100659.

(16) Stephens, N. M.; Smith, E. A. Structure of Deep Eutectic Solvents (DESs): What We Know, What We Want to Know, and Why We Need to Know It. *Langmuir* **2022**, *38*, 14017–14024.

(17) Stefanovic, R.; Ludwig, M.; Webber, G. B.; Atkin, R.; Page, A. J. Nanostructure, Hydrogen Bonding and Rheology in Choline Chloride Deep Eutectic Solvents as a Function of the Hydrogen Bond Donor. *Phys. Chem. Chem. Phys.* **2017**, *19*, 3297–3306.

(18) Tiecco, M.; Cappellini, F.; Nicoletti, F.; Del Giacco, T.; Germani, R.; Di Profio, P. Role of the Hydrogen Bond Donor Component for a Proper Development of Novel Hydrophobic Deep Eutectic Solvents. *J. Mol. Liq.* **2019**, *281*, 423–430.

(19) Abbasi, N. M.; Farooq, M. Q.; Anderson, J. L. Investigating the Variation in Solvation Interactions of Choline Chloride-Based Deep Eutectic Solvents Formed Using Different Hydrogen Bond Donors. *ACS Sustainable Chem. Eng.* **2021**, *9*, 11970–11980.

(20) Mjalli, F. S.; Ahmed, O. U. Characteristics and Intermolecular Interaction of Eutectic Binary Mixtures: Reline and Glyceline. *Korean J. Chem. Eng.* **2016**, *33*, 337–343.

(21) Pal, S.; Roy, R.; Paul, S. Potential of a Natural Deep Eutectic Solvent, Glyceline, in the Thermal Stability of the Trp-Cage Mini-Protein. *J. Phys. Chem. B* **2020**, *124*, 7598–7610.

(22) Fraenza, C. C.; Elgammal, R. A.; Garaga, M. N.; Bhattacharyya, S.; Zawodzinski, T. A.; Greenbaum, S. G. Dynamics of Glyceline and Interactions of Constituents: A Multitechnique NMR Study. *J. Phys. Chem. B* **2022**, *126*, 890–905.

(23) Yadav, A.; Trivedi, S.; Rai, R.; Pandey, S. Densities and Dynamic Viscosities of (Choline Chloride+glycerol) Deep Eutectic Solvent and Its Aqueous Mixtures in the Temperature Range (283.15–363.15)K. *Fluid Phase Equilibria* **2014**, *367*, 135–142.

(24) Faraone, A.; Wagle, D. V.; Baker, G. A.; Novak, E. C.; Ohl, M.; Reuter, D.; Lunkenheimer, P.; Loidl, A.; Mamontov, E. Glycerol Hydrogen-Bonding Network Dominates Structure and Collective Dynamics in a Deep Eutectic Solvent. *J. Phys. Chem. B* **2018**, *122*, 1261–1267.

(25) Kim, K.-S.; Park, B. H. Volumetric Properties of Solutions of Choline Chloride + Glycerol Deep Eutectic Solvent with Water, Methanol, Ethanol, or Iso-Propanol. *J. Mol. Liq.* **2018**, *254*, 272–279.

(26) Leron, R. B.; Li, M.-H. Molar Heat Capacities of Choline Chloride-Based Deep Eutectic Solvents and Their Binary Mixtures with Water. *Thermochim. Acta* **2012**, *530*, 52–57.

(27) Pandey, A.; Rai, R.; Pal, M.; Pandey, S. How Polar Are Choline Chloride-Based Deep Eutectic Solvents? *Phys. Chem. Chem. Phys.* **2014**, *16*, 1559–1568.

(28) Weeraratna, C.; Amarasinghe, C.; Lu, W.; Ahmed, M. A Direct Probe of the Hydrogen Bond Network in Aqueous Glycerol Aerosols. *J. Phys. Chem. Lett.* **2021**, *12*, 5503–5511.

(29) Turner, A. H.; Holbrey, J. D. Investigation of Glycerol Hydrogen-Bonding Networks in Choline Chloride/Glycerol Eutectic-Forming Liquids Using Neutron Diffraction. *Phys. Chem. Chem. Phys.* **2019**, *21*, 21782–21789.

(30) Ahmadi, R.; Hemmateenejad, B.; Safavi, A.; Shojaeifard, Z.; Shahsavar, A.; Mohajeri, A.; Heydari Dokoohaki, M.; Zolghadr, A. R. Deep Eutectic–Water Binary Solvent Associations Investigated by Vibrational Spectroscopy and Chemometrics. *Phys. Chem. Chem. Phys.* **2018**, *20*, 18463–18473.

(31) Baz, J.; Held, C.; Pleiss, J.; Hansen, N. Thermophysical Properties of Glyceline–Water Mixtures Investigated by Molecular Modelling. *Phys. Chem. Chem. Phys.* **2019**, *21*, 6467–6476.

(32) Ferreira, A. S. D.; Craveiro, R.; Duarte, A. R.; Barreiros, S.; Cabrita, E. J.; Paiva, A. Effect of Water on the Structure and Dynamics of Choline Chloride/Glycerol Eutectic Systems. *J. Mol.*

*Liq.* **2021**, *342*, 117463.

(33) Sajjadur Rahman, M.; Kyeremateng, J.; Saha, M.; Asare, S.; Uddin, N.; Halim, M. A.; Raynie, D. E. Evaluation of the Experimental and Computed Properties of Choline Chloride-Water Formulated Deep Eutectic Solvents. *J. Mol. Liq.* **2022**, *350*, 118520.

(34) Töpfer, K.; Pasti, A.; Das, A.; Salehi, S. M.; Vazquez-Salazar, L. I.; Rohrbach, D.; Feurer, T.; Hamm, P.; Meuwly, M. Structure, Organization, and Heterogeneity of Water-Containing Deep Eutectic Solvents. *J. Am. Chem. Soc.* **2022**, *144*, 14170–14180.

(35) Zhang, Q.; De Oliveira Vigier, K.; Royer, S.; Jérôme, F. Deep Eutectic Solvents: Syntheses, Properties and Applications. *Chem. Soc. Rev.* **2012**, *41*, 7108.

(36) Smith, E. L.; Abbott, A. P.; Ryder, K. S. Deep Eutectic Solvents (DESs) and Their Applications. *Chem. Rev.* **2014**, *114*, 11060–11082.

(37) Duan, L.; Dou, L.-L.; Guo, L.; Li, P.; Liu, E.-H. Comprehensive Evaluation of Deep Eutectic Solvents in Extraction of Bioactive Natural Products. *ACS Sustainable Chem. Eng.* **2016**, *4*, 2405–2411.

(38) Cunha, S. C.; Fernandes, J. O. Extraction Techniques with Deep Eutectic Solvents. *TrAC, Trends Anal. Chem.* **2018**, *105*, 225–239.

(39) D'Agostino, C.; Harris, R. C.; Abbott, A. P.; Gladden, L. F.; Mantle, M. D. Molecular Motion and Ion Diffusion in Choline Chloride Based Deep Eutectic Solvents Studied by 1H Pulsed Field Gradient NMR Spectroscopy. *Phys. Chem. Chem. Phys.* **2011**, *13*, 21383.

(40) D'Agostino, C.; Gladden, L. F.; Mantle, M. D.; Abbott, A. P.; Ahmed, E., I.; Al-Murshedi, A. Y. M.; Harris, R. C. Molecular and Ionic Diffusion in Aqueous – Deep Eutectic Solvent Mixtures: Probing Inter-Molecular Interactions Using PFG NMR. *Phys. Chem. Chem. Phys.* **2015**, *17*, 15297–15304.

(41) Dziubinska-Kühn, K.; Pupier, M.; Matysik, J.; Viger-Gravel, J.; Karg, B.; Kowalska, M. Time-Dependent Hydrogen Bond Network Formation in Glycerol-Based Deep Eutectic Solvents. *ChemPhysChem* **2022**, *23*, e202100806.

(42) Zhu, S.; Li, H.; Zhu, W.; Jiang, W.; Wang, C.; Wu, P.; Zhang, Q.; Li, H. Vibrational Analysis and Formation Mechanism of Typical Deep Eutectic Solvents: An Experimental and Theoretical Study. *J. Mol.Graph.* **2016**, *68*, 158–175.

(43) Pandey, A.; Pandey, S. Solvatochromic Probe Behavior within Choline Chloride-Based Deep Eutectic Solvents: Effect of Temperature and Water. *J. Phys. Chem. B* **2014**, *118*, 14652–14661.

(44) Elderderi, S.; Wils, L.; Leman-Loubière, C.; Henry, S.; Byrne, H. J.; Chourpa, I.; Munnier, E.; Elbashir, A. A.; Boudesocque-Delaye, L.; Bonnier, F. Comparison of Raman and Attenuated Total Reflectance (ATR) Infrared Spectroscopy for Water Quantification in Natural Deep Eutectic Solvent. *Anal. Bioanal. Chem.* **2021**, *413*, 4785–4799.

(45) Ramesh, R.; Nair, A.; Jayavel, A.; Sathiasivan, K.; Rajesh, M.; Ramaswamy, S.; Tamilarasan, K. Choline Chloride-Based Deep Eutectic Solvents for Efficient Delignification of Bambusa Bambos in Bio-Refinery Applications. *Chem. Pap.* **2020**, *74*, 4533–4545.

(46) Elbourne, A.; Meftahi, N.; Greaves, T. L.; McConville, C. F.; Bryant, G.; Bryant, S. J.; Christofferson, A. J. Nanostructure of a Deep Eutectic Solvent at Solid Interfaces. *J. Colloid Interface Sci.* **2021**, *591*, 38–51.

(47) Elbourne, A.; Besford, Q. A.; Meftahi, N.; Crawford, R. J.; Daeneke, T.; Greaves, T. L.;

McConville, C. F.; Bryant, G.; Bryant, S. J.; Christofferson, A. J. The Impact of Water on the Lateral Nanostructure of a Deep Eutectic Solvent–Solid Interface. *Aust. J. Chem.* **2021**, *75*, 111–125.

(48) Hammond, O. S.; Li, H.; Westermann, C.; Al-Murshedi, A. Y. M.; Endres, F.; Abbott, A. P.; Warr, G. G.; Edler, K. J.; Atkin, R. Nanostructure of the Deep Eutectic Solvent/Platinum Electrode Interface as a Function of Potential and Water Content. *Nanoscale Horiz.* **2019**, *4*, 158–168.

(49) Atilhan, M.; Costa, L. T.; Aparicio, S. Elucidating the Properties of Graphene–Deep Eutectic Solvents Interface. *Langmuir* **2017**, *33*, 5154–5165.

(50) Rozas, S.; Atilhan, M.; Aparicio, S. Deep Eutectic Solvent Reline at 2D Nanomaterial Interfaces. *J. Phys. Chem. B* **2020**, *124*, 1197–1206.

(51) García, G.; Atilhan, M.; Aparicio, S. Interfacial Properties of Deep Eutectic Solvents Regarding to $CO_2$ Capture. *J. Phys. Chem. C* **2015**, *119*, 21413–21425.

(52) Ullah, R.; Atilhan, M.; Anaya, B.; Khraisheh, M.; García, G.; ElKhattat, A.; Tariq, M.; Aparicio, S. A Detailed Study of Cholinium Chloride and Levulinic Acid Deep Eutectic Solvent System for $CO_2$ Capture via Experimental and Molecular Simulation Approaches. *Phys. Chem. Chem. Phys.* **2015**, *17*, 20941–20960.

(53) Gera, R.; Moll, C. J.; Bhattacherjee, A.; Bakker, H. J. Water-Induced Restructuring of the Surface of a Deep Eutectic Solvent. *J. Phys. Chem. Lett.* **2022**, *13*, 634–641.

(54) Ahmed, M.; Lu, W. Probing Complex Chemical Processes at the Molecular Level with Vibrational Spectroscopy and X-Ray Tools. *J. Phys. Chem. Lett.* **2023**, *14*, 9265–9278.

(55) Kostko, O.; Xu, B.; Jacobs, M. I.; Ahmed, M. Soft X-Ray Spectroscopy of Nanoparticles by Velocity Map Imaging. *J. Chem. Phys.* **2017**, *147*, 013931.

(56) Walz, M.-M.; Werner, J.; Ekholm, V.; Prisle, N. L.; Öhrwall, G.; Björneholm, O. Alcohols at the Aqueous Surface: Chain Length and Isomer Effects. *Phys. Chem. Chem. Phys.* **2016**, *18*, 6648–6656.

(57) Blundell, R. K.; Licence, P. Quaternary Ammonium and Phosphonium Based Ionic Liquids: A Comparison of Common Anions. *Phys. Chem. Chem. Phys.* **2014**, *16*, 15278–15288.

(58) Lee, M.-T.; Orlando, F.; Artiglia, L.; Chen, S.; Ammann, M. Chemical Composition and Properties of the Liquid–Vapor Interface of Aqueous C1 to C4 Monofunctional Acid and Alcohol Solutions. *J. Phys. Chem. A* **2016**, *120*, 9749–9758.

(59) Kostko, O.; Jacobs, M. I.; Xu, B.; Wilson, K. R.; Ahmed, M. Velocity Map Imaging of Inelastic and Elastic Low Energy Electron Scattering in Organic Nanoparticles. *J. Chem. Phys.* **2019**, *151*, 184702.

(60) Seah, M. P. An Accurate and Simple Universal Curve for the Energy-Dependent Electron Inelastic Mean Free Path: Simple, Accurate, Universal Expression for IMFPs. *Surf. Interface Anal.* **2012**, *44*, 497–503.

(61) Kumar, A.; Craig, V. S. J.; Page, A. J.; Webber, G. B.; Wanless, E. J.; Andersson, G. Ion Specificity in the Measured Concentration Depth Profile of Ions at the Vapor-Glycerol Interface. *J. Colloid Interface Sci.* **2022**, *626*, 687–699.

(62) Ashworth, C. R.; Matthews, R. P.; Welton, T.; Hunt, P. A. Doubly Ionic Hydrogen Bond Interactions within the Choline Chloride–Urea Deep Eutectic Solvent. *Phys. Chem. Chem. Phys.*

**2016**, *18*, 18145–18160.

(63) Křepelová, A.; Huthwelker, T.; Bluhm, H.; Ammann, M. Surface Chemical Properties of Eutectic and Frozen NaCl Solutions Probed by XPS and NEXAFS. *ChemPhysChem* **2010**, *11*, 3859–3866.

(64) Akutsu, H. Direct Determination by Raman Scattering of the Conformation of the Choline Group in Phospholipid Bilayers. *Biochemistry* **1981**, *20*, 7359–7366.

(65) Araujo, C. F.; Coutinho, J. A. P.; Nolasco, M. M.; Parker, S. F.; Ribeiro-Claro, P. J. A.; Rudić, S.; Soares, B. I. G.; Vaz, P. D. Inelastic Neutron Scattering Study of Reline: Shedding Light on the Hydrogen Bonding Network of Deep Eutectic Solvents. *Phys. Chem. Chem. Phys.* **2017**, *19*, 17998–18009.

(66) Chai, K.; Lu, X.; Zhou, Y.; Liu, H.; Wang, G.; Jing, Z.; Zhu, F.; Han, L. Hydrogen Bonds in Aqueous Choline Chloride Solutions by DFT Calculations and X-Ray Scattering. *J. Mol. Liq.* **2022**, *362*, 119742.

(67) de Souza, Í. F. T.; Ribeiro, M. C. C. A Raman Spectroscopy and Rheology Study of the Phase Transitions of the Ionic Liquid Choline Acetate. *J. Mol. Liq.* **2021**, *322*, 114530.

(68) de Souza, Í. F. T.; Paschoal, V. H.; Bernardino, K.; Lima, T. A.; Daemen, L. L.; Z, Y.; Ribeiro, M. C. C. Vibrational Spectroscopy and Molecular Dynamics Simulation of Choline Oxyanions Salts. *J. Mol. Liq.* **2021**, *340*, 117100.

(69) Weng, L.; Toner, M. Janus-Faced Role of Water in Defining Nanostructure of Choline Chloride/Glycerol Deep Eutectic Solvent. *Phys. Chem. Chem. Phys.* **2018**, *20*, 22455–22462.

(70) Wang, H.; Liu, S.; Zhao, Y.; Wang, J.; Yu, Z. Insights into the Hydrogen Bond Interactions in Deep Eutectic Solvents Composed of Choline Chloride and Polyols. *ACS Sustainable Chem. Eng.* **2019**, *7*, 7760–7767.

(71) Liu, D.; Ma, G.; Levering, L. M.; Allen, H. C. Vibrational Spectroscopy of Aqueous Sodium Halide Solutions and Air−Liquid Interfaces: Observation of Increased Interfacial Depth. *J. Phys. Chem. B* **2004**, *108*, 2252–2260.

(72) Grass, M. E.; Karlsson, P. G.; Aksoy, F.; Lundqvist, M.; Wannberg, B.; Mun, B. S.; Hussain, Z.; Liu, Z. New Ambient Pressure Photoemission Endstation at Advanced Light Source Beamline 9.3.2. *Rev. Sci. Instrum.* **2010**, *81*, 053106.

(73) Head, A. R.; Nemšák, S. Strategies for the Collection, Analysis and Interpretation of APXPS Data. In *ACS Symposium Series*; Head, A. R., Nemšák, S., Eren, B., Eds.; American Chemical Society: Washington, DC, 2021; Vol. 1396, pp 297–313.

(74) Jacobs, M. I.; Xu, B.; Kostko, O.; Wiegel, A. A.; Houle, F. A.; Ahmed, M.; Wilson, K. R. Using Nanoparticle X-Ray Spectroscopy to Probe the Formation of Reactive Chemical Gradients in Diffusion-Limited Aerosols. *J. Phys. Chem. A* **2019**, *123*, 6034–6044.